

A TOPAS Simulation of High-resolution Low-Z-Medium Whole-Body TOF-PET

Kepler Domurat-Sousa, Cameron Poe, João F. Shida, Eric Spiegler, Evelyn Sun, Bernhard W. Adams, Evan Angelico Henry J. Frisch, Patrick La Riviere, Allison Squires
to be submitted to Medical Physics: The International Journal of Medical Physics Research and Practice

Abstract

We have used the TOPAS Geant4-based simulation package to simulate a TOF-PET system employing a low atomic number liquid medium such as a photoswitchable organic scintillator rather than the conventional high-Z crystals. In a low atomic number medium the Compton scattering of a gamma from the positron annihilation dominates the absorption via the photo-electric effect, resulting in a chain of scatterings at successively lower gamma energies, each producing a recoil Compton electron that deposits ionization energy along its track. Multiple scattering and rate of ionization (dE/dx) depend on electron velocity and so can be used to identify the start of the recoil electron track at one end-point of the Line-of-Response (LOR).

The TOPAS package was used to simulate a cylindrical detector consisting of xx -cm thick xxx surrounding a bore diameter of xxx cm and covering the range in polar angle $-xxx^\circ - xxx^\circ$, filled with linear alkylbenzene (LAB) liquid scintillator as the ionization medium. Optical high resolution reconstruction remains to be developed; one example being explored is a low concentration (e.g. 10^{-xxx}) of a (hypothetical) photoswitchable dye. The LOR in each event was reconstructed via a time-ordering of the energy deposited by the successive Compton electrons.

Simulations have been performed for the Derenzo phantom and XCAT brain and lung phantoms to determine event reconstruction efficiencies, transverse resolutions, and image signal-to-noise. Mis-reconstructed events have a lower contrast than events with both ends of the LOR correctly identified by several orders-of-magnitude, forming a smooth background that is subtracted via a maximum likelihood fit to an expansion in Zernike functions. Locating the annihilation longitudinally on the LOR is implemented by large-area fast time-of-flight photodetectors with single photon time resolution in the tens of ps and sub-mm spatial resolution. In-patient scattering is rejected with efficiencies of xxx and xxx for the XCAT brain and lung phantoms, respectively. The simulations indicate a possible large reduction of dose. The development of suitable photoswitchable dyes or other image-persistent economical low-Z media may be possible.

Contents

1	Introduction	6
2	The TOPAS Geant4-based Simulation Framework	8
2.1	Functional description of the simulation	8
2.1.1	Overview of flow	8
2.1.2	Input	8
2.1.3	Custom additions to TOPAS	9
2.1.4	Output data: energy, position, time, particle-type, particle index, parent process	9
2.1.5	Custom additions- Cherenkov emission, positron scattering	9
2.1.6	Limitations, approximations, missing processes	10
2.2	Post simulation processing	10
2.3	XCAT phantoms	10
3	Simulating a model low-Z whole-Body TOF-PET Detector	10
3.1	Detector Geometry	11
3.2	Scintillating Media	11
3.3	Characteristics of the Compton Chain of Successive Scatters	11
3.3.1	Compton scattering 2-body kinematics	12
3.3.2	Reconstructing the chain of successive Compton scatterings from the TOPAS simulation	13
3.3.3	Containment and back-scattering	13
4	Reconstructing the Line-of-Response	15
4.1	Finding the recoil electron track from the first scatter of the gamma	15
4.2	Finding the point of first scatter in the electron track	15
4.3	Misidentified first scattering points	15
4.4	Reconstruction efficiencies for signal, in-patient scattering, and mis-reconstructed events	15
4.5	Transverse Resolution σ_T	16
4.5.1	Both LOR endpoints correctly identified	16
4.5.2	Misidentified LOR endpoints	16
5	Rejection of in-patient scattering	16
6	TOF resolution	17
7	Needle Stacking, Filtering, and Feature Recognition	18
7.1	Needle Stacking	18
7.2	Filtering	18
7.3	Feature Recognition	18
8	Imaging the Derenzo and XCAT Phantoms: Signal-to-Noise at reduced dose	19
8.1	Zernicke fits to low-frequency background	19

8.2	Derenzo Phantom	19
8.2.1	Signal-to-Noise at reduced dose	19
8.3	XCAT brain phantom	19
8.3.1	Signal-to-Noise for the XCAT brain phantom at reduced dose	19
9	Summary and Prospects	21
10	Appendix A: Cluster Finding	21
11	Acknowledgements	25

List of Figures

1	A TOPAS representation of a TOF-PET detector with a superposed simulated annihilation event in the patient.	7
2	The simulated electron tracks in a detector module corresponding to the chain of successive gamma-e Compton scatterings initiated by a 511 keV gamma from the e^+e^- annihilation in the patient.	7
3	The path of the electron from a high energy scattering event. Using the increasingly twisty path of the electron as it has lower energy the origin of the electron can be determined.	8
4	Data from TOPAS showing the displacement and energy of positrons at annihilation. Both histograms are from runs with 50000 positrons. Left: The distance traveled along the x-axis by positrons from their creation to their annihilation. Right: A log plot of the energy at annihilation of the positrons. The vast majority of positrons annihilate with no residual energy. In the zero bin 49584 of 49588 events are identically zero energy.	10
5	Distance in the detector medium traveled by: an initial 511 KeV gamma (black solid line); the outgoing gamma from the first Compton scattering (red dashed line); and the outgoing gamma from the 2nd Compton scattering (blue dotted line). T1 through T3 are the first through third true scatters.	12
6	The energy of the recoil electron versus the scattering angle for a 511 keV gamma as reconstructed by TOPAS, showing the kinematic constraint of 2-body scattering. The inset shows the profile at scattering angle of $\theta = 1.5$. xxxxxx The yellow line follows the theoretical prediction to within XXX	12
7	Left: xxx The fraction of successive Compton scatterings that deposit the highest energy (are ‘brightest’) of all scatterings. Right: xxx The distribution in energy deposited for the first scattering (rhomboids); the second scattering (squares); the third scattering (circles), and the fourth scattering (pentagons).	13
8	An example simulation of containment for a 30cm deep module with water as the medium, and a gamma entering at 45 degrees to the normal. Left: Number of scatters suffered by a gamma before escaping the module. Right: Energy deposited by a gamma before escaping the module for all scatters and the T_1 scatter.	14
9	Left: Histogram of TOF resolution from the first photon detected. Right: Integral of the TOF histogram, xxx% of Compton electrons have a TOF resolution lower than 270 ps.	18

10	Imaging the Derenzo phantom with the unfiltered back-projection of the needle stack. Left: The distribution of rods in the TOPAS model of the Derenzo phantom. The background was set to 5 MBq/kg and the rods to 15 MBq/kg. The exposure was set to 6 seconds, 1% of 10 minutes. Right: The output of needle stacking after the simulation. The colormap corresponds to how many needles are present at each location.	19
11	Imaging the XCAT brain phantom with the unfiltered back-projection of the needle stack. Left: the projected input source distribution density of annihilations with a 10-minute exposure using xxx Bq of ^{18}F in the rods and xxx Bq in the surrounding volume. Middle: the reconstructed projected image from summing the weights of needles crossing each voxel. Right: the reconstructed projected image after subtracting a least-mean-squares fit to the first xxx terms of an expansion in Zernike functions.	20
12	Comparisons of the reconstructed event after cluster finding and kinematic time-ordering with the true information from the simulation. a) The fraction of correct identifications of the reconstructed α (squares), β (circles); γ (rhomboids); and δ (crosses) clusters versus the true order N_i . b) Energy in cluster α vs in N_1 , in β vs in N_2 , in γ vs in N_3 , in δ vs in N_4 . c) The energy of the recoil electron versus the scattering angle in the N_1 scatter for the true first scatter ($N=1$) in solid circles and the reconstructed first scatter (β) in open circles. d) Distance to the entrance window for N_1 (squares); N_2 (circles); N_3 (rhomboids) scatters (solid symbols) and for the α, β, γ reconstructed ordering (open symbols). e) Distance between the true first interaction point of the gamma and the reconstructed interaction point for α (squares); β (circles); γ (rhomboids); and δ (crosses) clusters. f) The distribution in distance between the reconstructed and true annihilation points for the Derenzo phantom. The inset shows the distribution on an expanded scale to accommodate the broad distribution for misidentified clusters.	23
13	The corresponding three images of the Derenzo phantom from the parametric simulation shown in Fig. 10 but using a voxelized image and the simple seed-shoulder cluster finding algorithm [41, 20].	24

List of Tables

1	The result of successive selection criteria (cuts) on the TOPAS simulation sample for the Derenzo phantom, in per cent. The column labeled ‘cut’ is the percentage of events failing the listed cut. ‘Events’ is the cumulative percentage of surviving events; IPS is the percentage of Events which are have in-patient scatters; Mis-ID is the percentage of events for which one or both of the first interaction of the gamma is mis-identified. The requirement that both ends of the LOR be correctly identified corresponds to correctly identifying the start of the track of the first Compton electron for both legs. The Field-of-View row corresponds to the requirement that the LOR intersect the phantom;	16
---	---	----

2	The result of requiring the LOR lie in the scattering planes for the Derenzo phantom for three different values of the energy cut. The %-Cut column is the percentage of events surviving the listed cut. 'Events' is the cumulative total of events; IPS is the number of in-patient scatters; Mis-ID is the number of events for which one or both of the first interaction of the gamma is mis-identified. The row 'Polarization Weight' refers to a selection on the distribution in $\Delta\phi$ of the scattering planes.	17
---	---	----

1 Introduction

Precision Time-of-Flight Positron-Emission Tomography (TOF-PET) has become immensely sophisticated [1, 2, 3]. Among other innovations, state-of-the-art whole-body scanners have been built and characterized [4, 5], TOF-PET with sub-nanosecond coincidence [6] has recently been developed, an international competition to develop sub-10 ps TOF resolution [7] is now in place, and timing with resolutions of 10 psec or below using MCP-PMT photodetectors and Cherenkov light in pre-radiators [8, 9, 10] is being developed by Cherry et al. for higher spatial resolutions and lower doses [11].

A worthy goal for further TOF-PET development is to achieve resolutions set by the underlying physics processes rather than the detector segmentation [12]. In this context, we have been exploring PET scanners based on the development of fast large-area (400 cm^2) MCP-PMT-based photodetectors [13, 14, 15, 16] with low-cost high-speed waveform sampling data-acquisition [17, 18] viewing low atomic number scintillating media [19, 20, 21].

In a low atomic number scintillation medium such as an organic scintillator [38], the Compton scattering of a 511 keV gamma dominates absorption via the photo-electric effect by a factor of 10,000 [23], resulting in a chain of scatterings at successively lower gamma energies, each producing the track of a recoil electron in the detector medium. Measurement of the locations of the scatters, the relative angles between successive scatters, the plane of the scattering, and the deposited energies and directions of the recoil electrons allows using the kinematical constraints of the 2-body Compton scattering process to perform a statistical time-ordering of the gamma interactions.

Initial studies showed that reconstructing the recoil electron tracks may enable a time-ordering of the Compton scatterings in the detector, with a high probability of precisely identifying the site of the first interaction of each gamma [20]. Connecting the locations of the first interaction for both gammas provides the determination of the line-of-response (LOR) with a transverse resolution determined by the underlying physical processes. Additionally, large-area MCP-PMT-based photodetectors can provide cm-scale TOF resolution along the LOR [20]. The TOF system also measures the time and location of individual photons from the successive Compton scatterings and consequently allows disambiguation of multiple events. Optimizing images from the complex ensemble of locations, scattering planes, times, and energies in each event will require advanced analysis techniques beyond the scope of this work.

The scattering angles of the gamma and the energy of the scattered electron are determined by conservation of energy and momentum in the 2-body Compton process, providing handles on reconstructing the correct time-ordering. The earlier (higher energy) end of an electron track can be statistically determined from energy deposition and angular scattering. There are additional constraints from the requirement that the LOR connecting the 2 first-scatters must lie in the plane of the scattering determined by the angles and the electron track, and the angle between the two planes has a dependence predicted by the quantum entanglement of the two gamma polarizations. The TOF system may provide additional information constraining the time-ordering of the creation of the electrons.

There are candidate low-Z media that retain the imprint of local ionization through different persistence mechanisms, including those with a change in molecular states, and others in which the change is thermodynamic, as in a bubble chamber [24]. For a specific example, we have previously discussed the potential for development of appropriate two-state photoswitchable organic dyes [20]. In these cases energy resolutions on the order of a few

percent or less may be achievable [20].

In this present paper we present simulations using the TOPAS Geant4-based framework [25] of a TOPAS-generated whole-body TOF-PET detector similar to that of Ref [20]. TOPAS is much more user-friendly and transparent than the raw Geant4 used in our previous work. Topas also provides access for the user to add physics and analysis, as well as the opportunity to add code to extend and check the underlying physics. TOPAS also provides excellent user support.

The organization of the paper is as follows; Section 2 provides an introduction to TOPAS and describes the modifications for the whole-body TOF-PET analysis. Simulation results for the Derenzo phantom and an ideal detector are reported in Section 3. The analysis and results on TOF resolution are described in Section 6. Rejection of in-patient scattering through timing, gamma energy reconstruction, and the coplanarity and scattering plane correlations intrinsic in the 2-gamma emission from positron annihilation are presented in Section 5. The reconstruction of the LOR, including inefficiencies due to mis-reconstructions and geometric acceptance, are discussed in Section 4. Section 8 presents images and figures-of-merit for imaging the Derenzo phantom and the XCAT phantom of Alan Dershowitz [28]. A brief summary is given in Section 9.

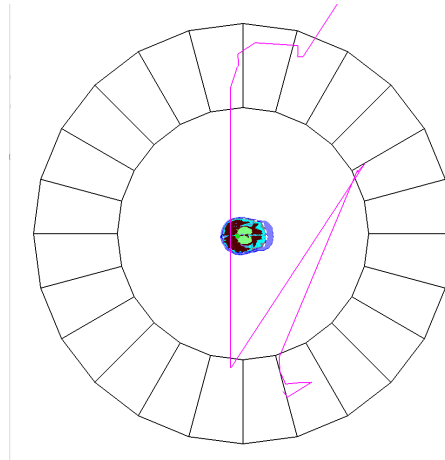


Figure 1: A TOPAS representation of a TOF-PET detector with a superposed simulated annihilation event in the patient.

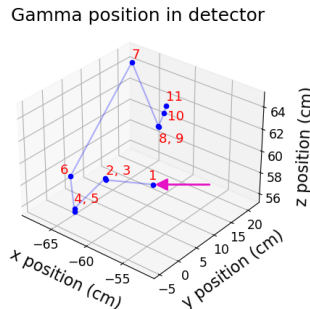


Figure 2: The simulated electron tracks in a detector module corresponding to the chain of successive gamma-e Compton scatterings initiated by a 511 keV gamma from the e^+e^- annihilation in the patient.

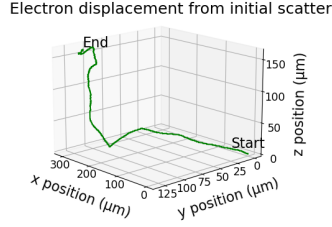


Figure 3: The path of the electron from a high energy scattering event. Using the increasingly twisty path of the electron as it has lower energy the origin of the electron can be determined.

2 The TOPAS Geant4-based Simulation Framework

(Kepler's section- suggested paragraphs one per line below)

Introduction to TOPAS w references;

Goals and guiding principles of the simulation implementation;

Modifications and compromises (e.g. simplified detector,...) for the results presented here.

TOPAS is a medical physics wrapper for Geant4. It allows for configuring Geant4 using text parameter files defining geometry, materials, particle sources and particle behavior recording.

TOPAS has allowed us to build a full simulation of a PET scanner with changeable phantoms.

Using a custom TOPAS scorer it was possible to get full data on particle interactions, allowing for the creation of a full simulation of event reconstruction.

2.1 Functional description of the simulation

The TOPAS simulation takes a description of a patient and detector and does all of the particle transport that results.

The result of the particle transport can then be input into reconstruction algorithms.

2.1.1 Overview of flow

The TOPAS simulation combines two parameter files: one defining the phantom and one defining the detector.

When run the simulation creates positrons within the phantom based on given activity data. TOPAS uses Geant4 to do the particle transport simulation, including any Compton scattering that occurs in the patient or detector.

The desired data is then output in a file recording particle location, energy, and identifying information. This file is then used for the reconstruction algorithms.

2.1.2 Input

(see Section 3.1)

The input is divided into two definitions: the detector definition and the phantom definition. Using TOPAS's system for file inclusion these can easily be changed independently.

The detector file defines the shape and material of the detector, along with how events occurring in it will be recorded.

The phantom file defines the shape, material, and activity of the phantom.

A Derenzo phantom was created using cylinders with varying activities. // not really sure how valuable it is to say how I defined the Derenzo. It's pretty obvious to anyone who has taken the TOPAS introduction course.

For a simulated patient the XCAT phantom was used. This is a 3d simulated patient with variation between tissues.

2.1.3 Custom additions to TOPAS

TOPAS allows for the creation of simulation aspects that are not a part of the software by default. In our case we needed information on particle location and energy within the detector.

The TOPAS extension framework allows direct contact with the underlying Geant4 for the specific cases where it is needed.

We created a custom tuple scorer for TOPAS that output particle energy, energy deposited in a step, position, and identifying information.

The custom scorer outputs the information for any geometry it is applied to. We typically made one file with particle data from the entire simulation, and a second only with information from inside the detector volume.

2.1.4 Output data: energy, position, time, particle-type, particle index, parent process

Reference to DocLib note/UC websites etc. on formats ?

Using the flexibility of TOPAS and the custom scorer we were able to quickly get various data we desired from Geant4.

We measured the behavior of positrons in our simulation by tracking the start and end of each positrons history in the custom scorer. By subtracting the starting position from the ending position we got the positron displacement behavior. By checking the energy prior to annihilation we determined how often Geant4 was giving annihilation with substantial residual momentum in the detector frame.

2.1.5 Custom additions- Cherenkov emission, positron scattering

We used the following particle transport modules "g4em-standard_opt4" and "g4em-penelope" TOPAS made the addition and removal of these packages the change of a single line of a parameter file. This allowed us to add the "g4optical" module to produce cherenkov light when measuring timing resolution in the modules.

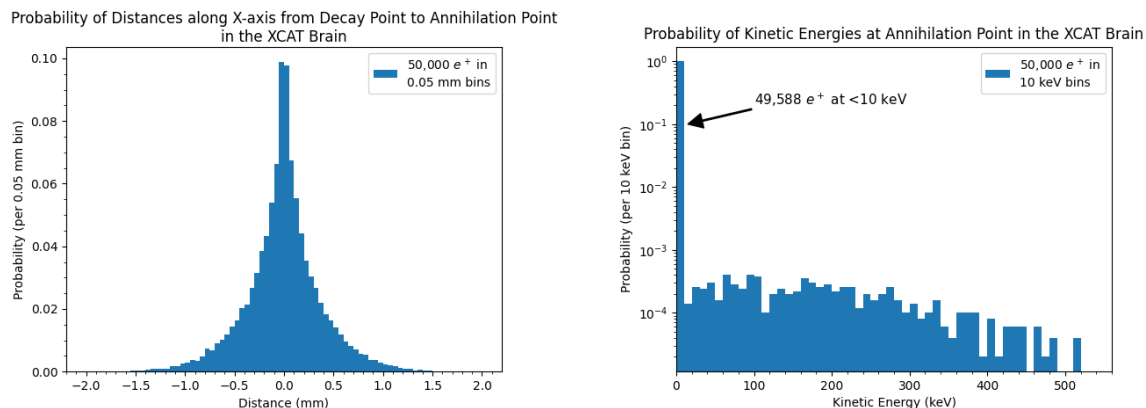


Figure 4: Data from TOPAS showing the displacement and energy of positrons at annihilation. Both histograms are from runs with 50000 positrons. Left: The distance traveled along the x-axis by positrons from their creation to their annihilation. Right: A log plot of the energy at annihilation of the positrons. The vast majority of positrons annihilate with no residual energy. In the zero bin 49584 of 49588 events are identically zero energy.

2.1.6 Limitations, approximations, missing processes

2.2 Post simulation processing

TOF. Cluster finding; Advanced methods, including adaptive weighting, other?

2.3 XCAT phantoms

The 4D Extended Cardiac-Torso (XCAT) Phantom Version 2.0 is a software program that can simulate detailed patient anatomies for use in medical imaging. XCAT outputs binary files of voxelized male and female phantoms representative of a 50th percentile U.S. adult. Further anatomical variation and customization options are available. In addition, XCAT can simulate cardiac plaque, cardiac defects, and arbitrary spherical lesions [29].

TOPAS can read ImageCube-formatted data to create voxelized geometry components. ImageCube-formatted data refers to any binary data that contains one value per voxel. For the case of XCAT, each value is a different XCAT material or tissue. TOPAS then allows the user to specify the density and atomic composition of each material in the phantom [cite topas site?].

Patient simulations in this paper use the male XCAT phantom with no anatomical variations from normal. For defining the materials in TOPAS, we used data for male adults from the Annals of the International Commission on Radiological Protection (ICRP) P89, P110, P145, and International Commission on Radiation Units and Measurements (ICRU) Report 46 [30, 31, 32, 33].

3 Simulating a model low-Z whole-Body TOF-PET Detector

We have previously described a whole-body TOF-PET scanner based on a low-Z medium containing a fast scintillator and a persistent medium such as a Switchillator photofluor [20].

We described a technique of time-ordering the Compton scatterings to precisely locate each end of the LOR, and the use of fast large-area TOF in a detector module. Here we present simulation results for an example whole-body detector, taking into account in-patient scattering (IPS), misidentifications, and detector resolutions.

Subsections 3.1 and 3.2 describe the model detector and the scintillating media, respectively. Subsection 3.3 describes determining the time-ordering of the Compton scatters in the ideal case by using the Compton kinematic constraints to find the location of first scattering. Table 1 presents the efficiencies for finding the the correct gamma interaction points, and hence the ends of the LOR at high resolution. Subsection 4.5 presents the extraction of the transverse resolution on the end-points.

An example of an implementation of the method beyond this parametric implementation is given in Appendix A, which presents the results of a voxelation of the detector volume and the reconstruction of the Compton recoil electron tracks by a shoulder-seed cluster-finding algorithm.

3.1 Detector Geometry

An example low-Z whole-body PET scanner with a simulated annihilation event from TOPAS superimposed is shown in Figure 1. The location of the annihilation is indicated by the star; the successive interactions in the detector by Compton scattering are indicated by the resulting electron tracks in the low-Z medium. The location of the first scatter of each gamma determines the corresponding end of the Line-of-Response, with the goal of a transverse resolution measured in tens of microns [20]. The superposition of many lines of response gives a point-spread function with the transverse resolution [20].

3.2 Scintillating Media

The scintillation medium assumed here comprises an organic solvent, a fast scintillator for the initial coincidence that triggers the data acquisition sequence, a photo-switchable dye that records the ionization from tracks of the Compton recoil electrons for repeated interrogation, and possible sensitizers to transfer energy from the solvent to the photo-switchable dye. We have taken the properties of the Kamland-Zen scintillator [22] for the simulation of the Compton chain. For the TOF simulation, we have assumed the fast scintillator has a 2 ps risetime [37] and a (single) decay time of xxx ps.

3.3 Characteristics of the Compton Chain of Successive Scatters

At 511 keV, the Compton scattering cross-section dominates the Photo-electric cross-section by a factor of 10^4 , resulting in a chain of successive Compton scatterings, with each one producing an ionizing electron and a gamma with lower energy. In the low-Z medium the scatterings are typically separated by distances of cm, several orders-of-magnitude larger than the intrinsic resolution. Figure 5 shows the results of the TOPAS simulation on the distance traveled in the medium to the next scattering by: 1) an incoming initial 511 keV gamma; 2) the gamma resulting from the first scattering; and 3) the gamma resulting from the second scattering. The peaking of the distribution for the initial gamma is due to the energy dependence of the Compton scattering cross-section

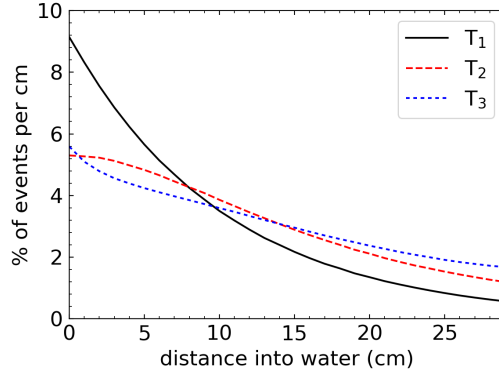


Figure 5: Distance in the detector medium traveled by: an initial 511 KeV gamma (black solid line); the outgoing gamma from the first Compton scattering (red dashed line); and the outgoing gamma from the 2nd Compton scattering (blue dotted line). T1 through T3 are the first through third true scatters.

3.3.1 Compton scattering 2-body kinematics

The 2-body kinematics of each scattering constrain the scattering angles and the outgoing energies [20]. The goal is to use the constraints to time-order the observed successive ionization sites to locate the first scatter, with the start of that ionizing track being one end of the LOR [20].

Fig. 6 shows the relationship between the gamma scattering angle and the recoil electron energy due to the 2-body Compton scattering kinematics for a 511 keV gamma. The inset shows the profile at scattering angle of $\theta = 0.71$ radians. The profile width is due to xxx.

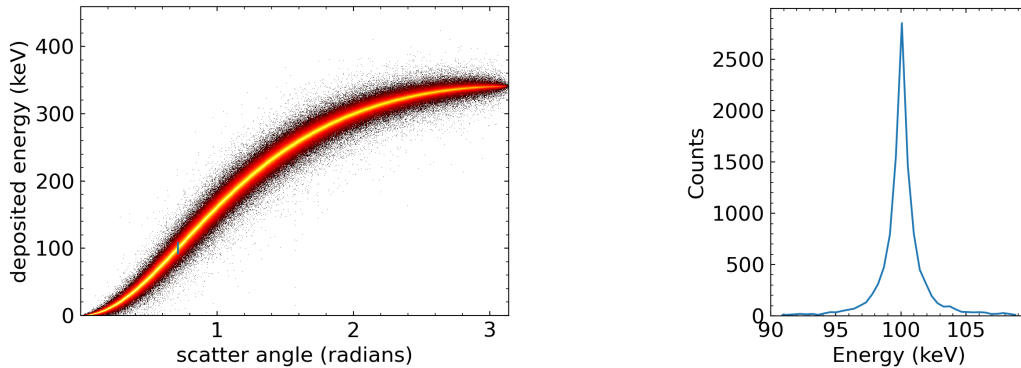


Figure 6: The energy of the recoil electron versus the scattering angle for a 511 keV gamma as reconstructed by TOPAS, showing the kinematic constraint of 2-body scattering. The inset shows the profile at scattering angle of $\theta = 1.5$. The yellow line follows the theoretical prediction to within XXX

3.3.2 Reconstructing the chain of successive Compton scatterings from the TOPAS simulation

We identify the order of the generated (true) scatterings by T followed by numbering ($T_1, T_2, \dots, T_i, \dots$), while the ordering of the scatterings as reconstructed from the analysis is labeled by R and numbering ($R_1, R_2, \dots, R_i, \dots$). For example, in this notation a successful reconstruction of an LOR end-point is when the R_1 reconstructed cluster is the generated cluster with ‘scatter index’ T_1 .

Figure 7 plots the fraction of time (%) the T_i th recoil electron track is the cluster with the highest deposited energy, i.e. the T_1 -scatter (rhomboids), the T_2 -scatter (squares), the T_3 -scatter (circles), and the T_4 -cluster (pentagons). The first scatter is the cluster with the highest energy for close to 60% of scatter, and the set of the T_1, T_2, T_3, T_4 energy depositions contains the first scatter in xxx % of gammas. Fig. ?? plots the distributions in energy deposited by the recoil electron for scatter index N_1 (squares); N_2 (circles); N_3 (rhomboids).

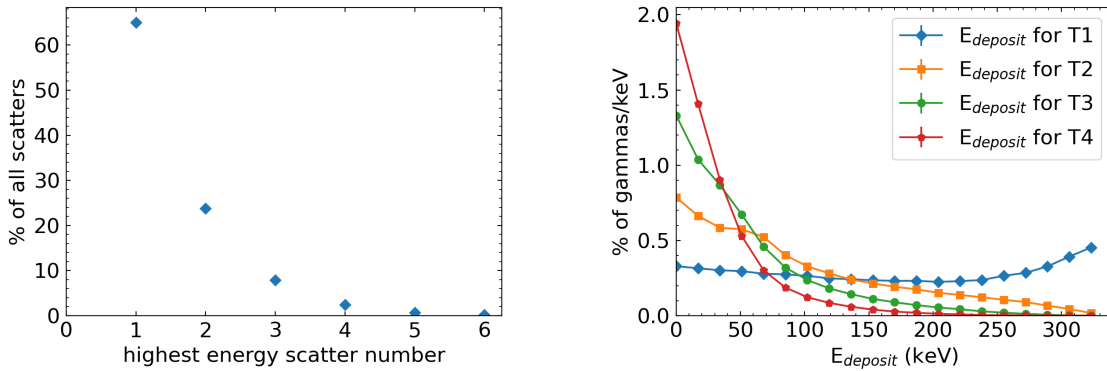


Figure 7: Left: xxx The fraction of successive Compton scatterings that deposit the highest energy (are ‘brightest’) of all scatterings. Right: xxx The distribution in energy deposited for the first scattering (rhomboids); the second scattering (squares); the third scattering (circles), and the fourth scattering (pentagons).

3.3.3 Containment and back-scattering

The many-cm pathlength between Compton scatterings and the large angular range of the outgoing gamma result in substantial inter-module scattering and escaped gamma due to backscattering ¹. The number of scatters suffered by a gamma before escaping the module is shown in the left-hand panel of Fig. 8. The energy deposited by a gamma before escaping the module is shown in the right-hand panel for both all scatters and for the T_1 scatter.

¹We note that back-scattering produces the highest energy electrons, leading to good resolution on electron direction and starting point.

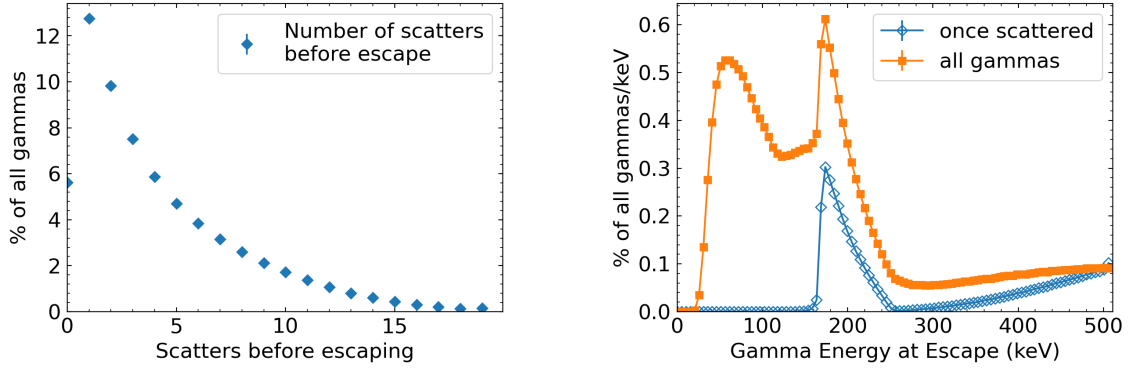


Figure 8: An example simulation of containment for a 30cm deep module with water as the medium, and a gamma entering at 45 degrees to the normal. Left: Number of scatters suffered by a gamma before escaping the module. Right: Energy deposited by a gamma before escaping the module for all scatters and the T_1 scatter.

4 Reconstructing the Line-of-Response

The TOPAS simulation allows us to estimate the reconstruction efficiencies, backgrounds, and resolution using a cut-based parametric analysis ².

4.1 Finding the recoil electron track from the first scatter of the gamma

Each end point of the LOR is found by cycling over the 10xxx highest-energy tracks in the triggering module and its neighbors, calculating a goodness-of-fit to the kinematic constraints for each combination. The figure of merit is

$$\chi^2 = \Sigma etc. \quad (1)$$

where the uncertainties in energy and angle are xxx and xxx, respectively.

4.2 Finding the point of first scatter in the electron track

For an as-yet unscattered gamma, the trajectory, and hence the LOR, ends at the start of the recoil electron track. The simulation accounts for multiple-scattering and energy loss along the electron track. We use the evolution of these two processes as the electron energy decreases along the track to determine which end of the track is the site of the gamma scattering. The figure of merit is:

$$\chi^2 = \Sigma Compton energy uncertainty formula \quad (2)$$

where the uncertainties in energy and angle are δ_E and δ_θ , respectively.

The scatters are used to form a tree of possible paths. If there are more than 10 scatters, the lowest energy scatters are ignored. All paths starting from the remaining scatters are tried. The search works by xxx a description of the tree behavior, including far side requirements. Possibly also include α, β pruning?

4.3 Misidentified first scattering points

A feature of the large disparity between the transverse resolution σ_T (10's of microns) and the scale of the separation between successive scatters (10's of cm) is that tracks misidentified as first scatters have LORs that miss by cm, and so form a low-frequency low-contrast background to the high-contrast correct orderings. This background is subtracted in the maximum likelihood fit to lower orders of a set of complete functions (see Section 8.1).

4.4 Reconstruction efficiencies for signal, in-patient scattering, and mis-reconstructed events

Table 1 presents the percentage of annihilation events from two-gamma signal, in-patient scattering (IPS), and mis-reconstruction (MisID) that survive successive selection criteria.

²In contrast to the parametric analysis, an analysis based on a voxelized volume, simulated electron tracks, and a seed-shoulder based clustering algorithm is presented in Appendix A.

The table presents three values for the energy cut: 5%, 2%, and 1%. The final efficiency for correctly identifying both ends of the LOR signal are xxx%, xxx%, and xxx% for the three energy cuts, respectively. The percentages of background remaining in the samples are xxx%, xxx%, and xxx%, respectively.

Derenzo Phantom						
Step	Selection	Cut	Cumulative	Signal	IPS	MisID
0	None	0%	100%	NA	xxx	xxx
1	Trigger- $\Delta\phi\theta$	xxx	xxx	xxx	xxx	xxx
2	First Clstr 1 leg					
3	First Clstr 2 legs					
4	Both Ends of LOR correct					
5	Field-of-View					
6a	$\Delta-E < 5\%$ 1 leg					
7a	$\Delta-E < 5\%$ 2 legs					
6b	$\Delta-E < 2\%$ 1 leg					
7b	$\Delta-E < 2\%$ 2 legs					
6c	$\Delta-E < 1\%$ 1 leg					
7c	$\Delta-E < 1\%$ 2 legs					

Table 1: The result of successive selection criteria (cuts) on the TOPAS simulation sample for the Derenzo phantom, in per cent. The column labeled ‘cut’ is the percentage of events failing the listed cut. ‘Events’ is the cumulative percentage of surviving events; IPS is the percentage of Events which are have in-patient scatters; Mis-ID is the percentage of events for which one or both of the first interaction of the gamma is mis-identified. The requirement that both ends of the LOR be correctly identified corresponds to correctly identifying the start of the track of the first Compton electron for both legs. The Field-of-View row corresponds to the requirement that the LOR intersect the phantom;

4.5 Transverse Resolution σ_T

The transverse resolution on the correctly reconstructed LORs is determined by the multiple scattering of the positron before annihilation, the momentum transfer to the e^+e_- system by the positron at annihilation, diffusion of the ionization before readout and the optical resolution of the repeated fluorescing of the Switchillator [44]. We take

4.5.1 Both LOR endpoints correctly identified

4.5.2 Misidentified LOR endpoints

5 Rejection of in-patient scattering

As described in Section 3.3, the reconstruction of the Compton chain introduces new methods for rejecting in-patient scattering beyond the conventional 511 keV energy cut on the deposited energy. First, the LOR must lie in the planes of the first scatter of each gamma. Second, due to the $\cos(\phi)$ dependence of the Compton scattering cross-section, where ϕ is

measured from the polarization, and the entanglement of the two gammas which typically arise from the singlet state of positronium, the angle $\Delta\phi$ between the two scattering planes is a discriminant against the flat distribution from background. We present the background rejection from a cut that is 90% efficient for signal (i.e. unscattered events).

Table 2 summarizes the effect of requiring the LOR lie in the scattering planes for the Derenzo phantom for three different values of the energy cut. The %-Cut column is the percentage of events surviving the listed cut. ‘Events’ is the cumulative total of events; IPS is the number of in-patient scatters; Mis-ID is the number of events for which one or both of the first interaction of the gamma is mis-identified. The row ‘Polarization Weight’ refers to a selection on the distribution in $\Delta\phi$ of the scattering planes of the two gammas at 90% efficiency for signal.

In-Patient Scattering Rejection: Derenzo Phantom						
Step	Cut	% Cut	Events	Signal	IPS	MisID
0	Event Selection $\Delta\text{-E} < 5\%$	NA	xxx	NA	xxx	xxx
1	LOR Out-of-Plane	xxx	xxx	xxx	xxx	xxx
2	Polarization Weight	xxx	xxx	xxx	xxx	xxx
0	Event Selection $\Delta\text{-E} < 2\%$	NA	xxx	NA	xxx	xxx
1	LOR Out-of-Plane	xxx	xxx	xxx	xxx	xxx
2	Polarization Weight	xxx	xxx	xxx	xxx	xxx
0	Event Selection $\Delta\text{-E} < 1\%$	NA	xxx	NA	xxx	xxx
1	LOR Out-of-Plane	xxx	xxx	xxx	xxx	xxx
2	Polarization Weight	xxx	xxx	xxx	xxx	xxx

Table 2: The result of requiring the LOR lie in the scattering planes for the Derenzo phantom for three different values of the energy cut. The %-Cut column is the percentage of events surviving the listed cut. ‘Events’ is the cumulative total of events; IPS is the number of in-patient scatters; Mis-ID is the number of events for which one or both of the first interaction of the gamma is mis-identified. The row ‘Polarization Weight’ refers to a selection on the distribution in $\Delta\phi$ of the scattering planes.

6 TOF resolution

The Time-of-Flight (TOF) system that was simulated consists of a large-area fast ($\sigma < 25$ psec) photo-detector with spatial resolution less than a few mm, such as an MCP-PMT-based LAPPDTM or an array of SiPMTs, augmented by a reflective surface on the inner surface of the entrance window [20].

In contrast to the localization of the chain of successive Compton scatterings, the measurements of the times of each of the two gammas has to be done using prompt light from the fast scintillator component of the detector medium. However the locations of the gamma scatterings can be used in the extraction of the interaction time.

A simple algorithm for determining the time is to use the time of the first photon detected, corrected for the path length between the position on the fast TOF detector (FD) and the location of the first gamma interaction measured in the Switchillator. Using the Kamland-Zen [22] scintillator as a model, we assume a light yield of xxx photons/MeV, a

rise-time of 2 psec [37], and a decay time of xxx psec. The simulation was run with two values of the quantum efficiency. 25%, conservative for typical bialkali cathodes [36], and 50%, optimistic for solid state devices [34].

In addition, it may be possible to individually correlate the prompt photons with the locations identified by the persistent medium with a finely pixelated large-area MCP-PMT-based photodetector recording the expanding spherical shell of photons from the recoil electron track to measure the time and position of the source [35]. Precise measurements of the positions of the photons at the photocathode face and the cluster locations in the medium may allow a 1-parameter fit for the time of each cluster [42].

Figure 9 shows the resulting differential and integral distributions of the single-gamma TOF resolution.

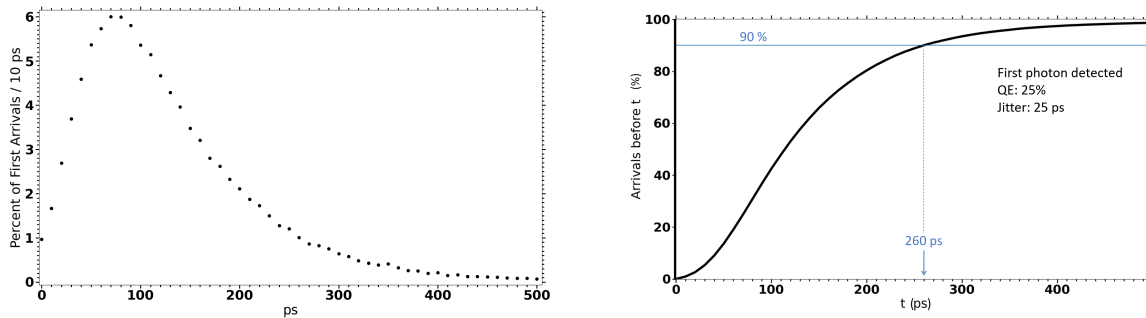


Figure 9: Left: Histogram of TOF resolution from the first photon detected. Right: Integral of the TOF histogram, xxx% of Compton electrons have a TOF resolution lower than 270 ps.

7 Needle Stacking, Filtering, and Feature Recognition

7.1 Needle Stacking

Andy's single continuous function?

7.2 Filtering

Low angular frequency due to 'accidental' pileup of needles

7.3 Feature Recognition

Brief (very) description of use of ML and AI on high-resolution images.

8 Imaging the Derenzo and XCAT Phantoms: Signal-to-Noise at reduced dose

8.1 Zernicke fits to low-frequency background

8.2 Derenzo Phantom

Description and reference for Derenzo phantom goes here

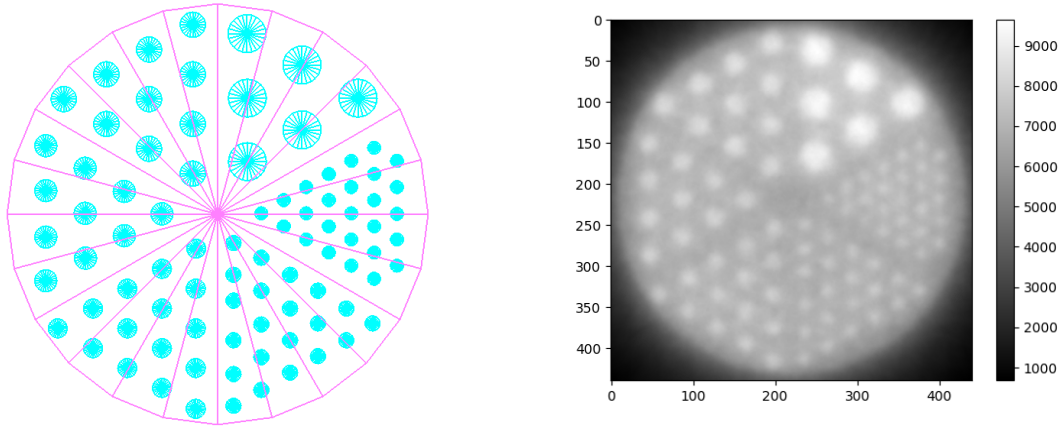


Figure 10: Imaging the Derenzo phantom with the unfiltered back-projection of the needle stack. Left: The distribution of rods in the TOPAS model of the Derenzo phantom. The background was set to 5 MBq/kg and the rods to 15 MBq/kg. The exposure was set to 6 seconds, 1% of 10 minutes. Right: The output of needle stacking after the simulation. The colormap corresponds to how many needles are present at each location.

8.2.1 Signal-to-Noise at reduced dose

Maximum likelihood fit to Derenzo phantom

Model and Free Parameters

S/N results

8.3 XCAT brain phantom

Hoffman brain reference (reasoning to 4:1 uptake)

Doses to white and grey matter, timing

Conversion to total positrons per cubic cm

Three figures: raw output, fourier filtered, fourier+zernike filtered

8.3.1 Signal-to-Noise for the XCAT brain phantom at reduced dose

Maximum likelihood fit to XCAT brain phantom

Model and Free Parameters

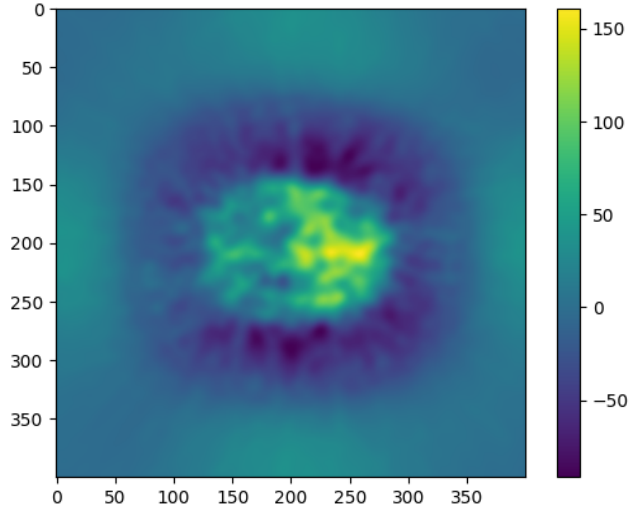


Figure 11: Imaging the XCAT brain phantom with the unfiltered back-projection of the needle stack. Left: the projected input source distribution density of annihilations with a 10-minute exposure using xxx Bq of ^{18}F in the rods and xxx Bq in the surrounding volume. Middle: the reconstructed projected image from summing the weights of needles crossing each voxel. Right: the reconstructed projected image after subtracting a least-mean-squares fit to the first xxx terms of an expansion in Zernike functions.

S/N results

9 Summary and Prospects

We have used the TOPAS simulation framework to characterize the performance of a TOF-PET detector based on an ionization-sensitive low-Z persistent medium and fast MCP-based photodetectors to record the chain of Compton scatterings of the annihilation gamma rays. The time-ordering of the successive gamma scatters in the chain is time-ordered using the energies and relative positions of the scatterings. In-patient scattering is identified by measuring the component of the LOR out of the scattering planes, the correlation of the polar angles resulting from the entanglement of the two gamma polarizations, and the reconstructed gamma energies. Results are presented for the XCAT brain and Derenzo phantoms.

The parametric simulation includes the effects of positron multiple-scattering before annihilation, localization of the first gamma interaction point at each end of the LOR, including which end is the start of the Compton recoil track, energy resolution, TOF resolution, in-patient scattering, and mis-identification of the first cluster in the chain.

We present images of the phantoms at a dose of xxx Bq/cc in the signal region of interest and a dose of xxx Bq/cc in the background. A signal-to-noise ratio of xxx and xxx are achieved for the Derenzo and XCAT phantoms, respectively.

We have in addition simulated a detector based on photo-switchable fluors [20] using a voxelized analysis in which the Compton electron tracks are reconstructed with a simple seed-shoulder cluster algorithm to measure the ionization and direction. A signal-to-noise ratio of xxx and xxx are achieved for the Derenzo and XCAT phantoms, respectively, lower than the ideal case by approximately xxx %.

The prospects for the technique depend on finding or developing an appropriate persistent low-Z medium. Among candidates, photo-switchable dyes in solution with a fast scintillator and energy-transfer-enhancing mediators may be possible [43].

10 Appendix A: Cluster Finding

The use of a persistent medium such as a Switchillator [20] allow multiple cycles of excitation and recording of the fluorescence for molecules activated by recoil electron ionization. Here we present a simulation of going beyond the ideal case above in reconstructing the time-ordered chain of scatterings to estimate the efficiencies for reconstructing the LOR.

The simulation code first voxelizes a volume of xxx by xxx mm containing the electron track, summing the energy deposited in each voxel (xxx- how does this work- xxx?). A clustering-algorithm links the eight adjacent voxels with energies over a ‘shoulder’ threshold [41, 20]. A higher ‘seed’ threshold is then applied to identify voxels to which the nearest-neighbor algorithm is applied. The resulting list of clusters is then curated to merge nearby clusters separated by a small number of missing voxels xxx can we be specific somewhere else? xxx.

In the following figures, we label the ordering of the true gamma scatterings by arabic numerals, i.e. 1, 2, ... N. The reconstructed clusters are ordered by Greek letters, with the cluster identified as being the first scatter being α , followed by β, γ etc. A correct identification of the first true scatter being correctly ordered is thus given by the frequency of matching the α cluster to the N=1 scatter.

Figure 12a plots the fraction of correct identifications of the reconstructed α (squares), β (circles); γ (rhomboids); and δ (crosses) clusters versus the true order N_i , after the kine-

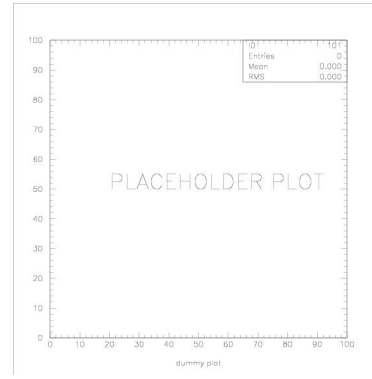
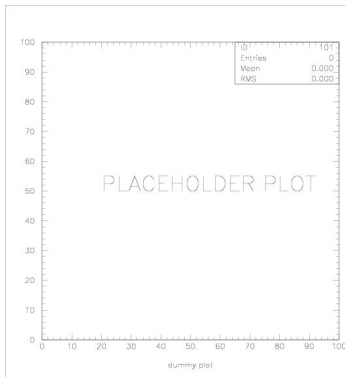
matic constraints to time-order the clusters have been applied. The correct first scatter is identified for xxx % of the gammas; the correct first scatter is included in the first three (α, β, γ reconstructed clusters xxx %).

Figure 12b shows the energy in cluster α versus the true energy in N_1 , in β vs in N_2 , in γ vs in N_3 , in δ vs in N_4 .

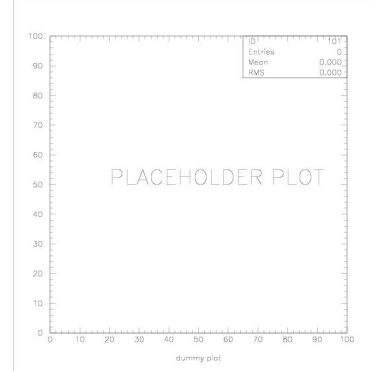
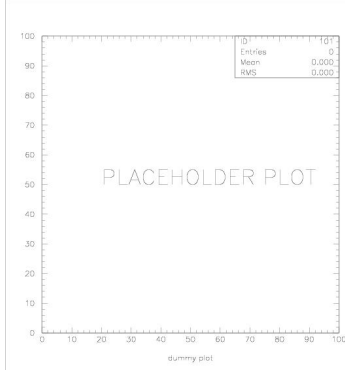
The energy of the recoil electron versus the scattering angle in the N_1 scatter for the true first scatter ($N=1$) in solid circles and the reconstructed first scatter (α) in open circles is displayed in Figure 12c.

Figure 12d displays the distance to the entrance window for N_1 (squares); N_2 (circles); N_3 (rhomboids) scatters (solid symbols) and for the α, β, γ reconstructed ordering (the corresponding open symbols).

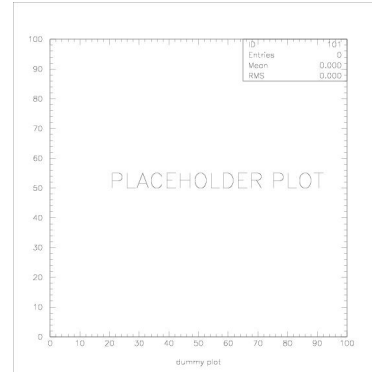
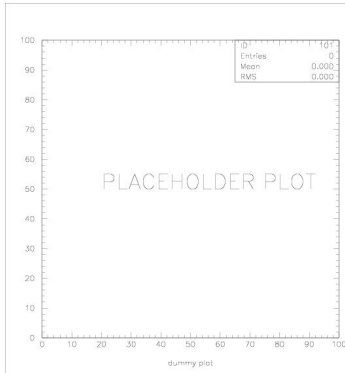
The distance between the true point of first interaction of the gamma and the reconstructed interaction point for α (squares); β (circles); γ (rhomboids); and δ (crosses) clusters is shown in Figure 12e. Figure 12f shows the distribution in distance between the reconstructed and true annihilation points for the Derenzo phantom. The inset shows the distribution on an expanded scale to accommodate the broad distribution for misidentified clusters.



(a) Fraction of correct identifications of reconstructed α (squares), β (circles); γ (rhomboids); (b) Energy in cluster α vs in N_1 , β vs in N_2 , γ vs and δ (crosses) clusters vs. the true order N_i . in N_3 , δ vs in N_4 .



(c) Energy of the recoil electron versus scattering angle in the N_1 scatter for the true first scatter (squares); N_2 (circles); N_3 (rhomboids) scatters ($N=1$) (solid) and reconstructed first scatter (β) (solid) and for the α, β, γ reconstructed ordering (open). (d) Distance to the entrance window for N_1 (squares); N_2 (circles); N_3 (rhomboids) scatters (solid symbols) and for the α, β, γ reconstructed ordering (open symbols).



(e) Distance between the true first interaction point of the gamma and the reconstructed point and the reconstructed point for α (squares); Derenzo phantom. The inset shows the distribution on an expanded scale to accommodate misidentified clusters. (f) Distribution in distance between reconstructed and true annihilation points for the point and the reconstructed point for α (squares); β (circles); γ (rhomboids); and δ (crosses) clusters.

Figure 12: Comparisons of the reconstructed event after cluster finding and kinematic time-ordering with the true information from the simulation.

a) The fraction of correct identifications of the reconstructed α (squares), β (circles); γ (rhomboids); and δ (crosses) clusters versus the true order N_i .

b) Energy in cluster α vs in N_1 , in β vs in N_2 , in γ vs in N_3 , in δ vs in N_4 .

c) The energy of the recoil electron versus the scattering angle in the N_1 scatter for the true first scatter ($N=1$) in solid circles and the reconstructed first scatter (β) in open circles.

d) Distance to the entrance window for N_1 (squares); N_2 (circles); N_3 (rhomboids) scatters (solid symbols) and for the α, β, γ reconstructed ordering (open symbols).

e) Distance between the true first interaction point of the gamma and the reconstructed point and the reconstructed point for α (squares); Derenzo phantom. The inset shows the distribution on an expanded scale to accommodate misidentified clusters.

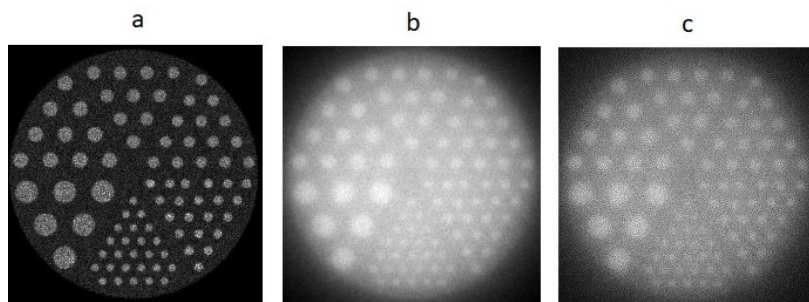


Figure 13: The corresponding three images of the Derenzo phantom from the parametric simulation shown in Fig. 10 but using a voxelized image and the simple seed-shoulder cluster finding algorithm [41, 20].

11 Acknowledgements

Christian Buck, Michael Gross, Mary Heinz, Yifan Zhao, Paul Segars

A. Squires was supported by the Neubauer Family Foundation and the University of Chicago Materials Research Science and Engineering Center, which is funded by the National Science Foundation under award number DMR-2011854. P. La Riviere was partially supported from NIH R01EB026300. The Geant4 simulation and code development by A. Elagin for neutrinoless double-beta decay were supported by the DOE under contract DE-SC0008172. Materials and supplies and support for drafting graphics were provided by the Physical Sciences Division (PSD) of the University of Chicago. The student authors were supported by the University's Enrico Fermi Institute, the College, and the PSD. This work made use of the shared facilities at the University of Chicago Materials Research Science and Engineering Center, supported by National Science Foundation under award number DMR-2011854

References

- [1] S. Vandenberghe, P. Moskal, J. S. Karp; *State of the art in total body PET* EJNMMI Phys. 2020 May 25;7(1):35.
doi: 10.1186/s40658-020-00290-2.
- [2] J. J. Vaquero and P. Kinahan; *Positron Emission Tomography: Current Challenges and Opportunities for Technological Advances in Clinical and Preclinical Imaging Systems* Annual Review of Biomedical Engineering Volume 17, 385; (2015)
- [3] M. E. Phelps, S. R. Cherry, and M. Dahlbom;
PET: Physics, instrumentation, and scanners; Springer New York
(2006)//doi.org/10.1007/0-387-34946-4
- [4] S. Vandenberghe, P. Moskal, J.S. Karp; *State of the art in total body PET* EJNMMI Phys. 2020 May 25;7(1):35.
doi: 10.1186/s40658-020-00290-2. PMID: 32451783; PMCID: PMC7248164.
- [5] R. D. Badawi, H. Shi, and S. R. Cherry et al.
First Human Imaging Studies with the EXPLORER Total-Body PET Scanner;
J Nucl Med. 2019 Mar; 60(3): 299-303. doi: 10.2967/jnumed.119.226498
- [6] M.S. Lee, J. Cates, A. Gonzalez-Montoro, and C. Levin;
High-resolution time-of-flight PET detector with 100 ps coincidence time resolution using a side-coupled phoswich configuration;
Phys. Med. Biol. in press: <https://doi.org/10.1088/1361-6560/ac01b5> (2021)
- [7] P. Lecoq, C. Morel and J. Prior, *Case for setting up a 10ps challenge: A step toward reconstruction-less TOF-PET*;
Nuovo Cim. C **43** (2020) no.1, 2 doi:10.1393/ncc/i2020-20002-y
- [8] T. Credo, H. Frisch, H. Sanders, R. Schroll, and F. Tang;
Picosecond Time-of-Flight Measurement for Colliders Using Cherenkov Light

- Proceedings of the IEEE, Rome, Italy, Oct. 2004; Nuclear Science Symposium Conference Record, 2004 IEEE, Vol. 1.
- [9] K. Inami, N. Kishimoto, Y. Enari, M. Nagamine, and T. Ohshima; *A 5-ps Tof-counter with an MCP-PMT*; Nucl. Instr. Meth. A560, p.303, 2006
 - [10] A. Ronzhin et al., *Development of a 10 ps level time of flight system in the Fermilab Test beam facility*; Nucl. Instr. Meth. A623,931(2010).
 - [11] R. Ota, S. I. Kwon, E. Berg, F. Hashimoto, K. Nakajima, I. Ogawa, Y. Tamagawa, T. Omura, T. Hasegawa, S. R. Cherry;
Direct positron emission imaging: ultra-fast timing enables reconstruction-free imaging
<https://arxiv.org/ftp/arxiv/papers/2105/2105.05805.pdf>
 - [12] W. W. Moses; *Fundamental Limits of Spatial Resolution in PET*; Nucl Instrum Methods Phys Res A. 2011 Aug 21;648 Supplement 1:S236-S240. doi: 10.1016/j.nima.2010.11.092.
 - [13] B. Adams et al.; *A Brief Technical History of the Large-Area Picosecond Photodetector (LAPPD) Collaboration*; arXiv:1603.01843
 - [14] B.W. Adams, A. Elagin, H. Frisch, R. Obaid, E. Oberla, A. Vostrikov, R. Wagner, J. Wang, M. Wetstein; *Timing Characteristics of Large Area Picosecond Photodetectors*; Nucl. Instr. Meth. Phys. Res. A. , Vol. 795, 1 (Sept. 2015).
 - [15] For a discussion of the factors that determine time and space resolution in MCP-based detectors, see the contributions to: *The Factors that Limit Time Resolution in Photodetectors*; Workshop, Univ. of Chicago, Chicago, IL; 28-29 April 2011. See <http://psec.uchicago.edu/workshops/>
 - [16] C. Aberle, A. Elagin, H.J. Frisch, M. Wetstein, L. Winslow; *Measuring Directionality in Double-Beta Decay and Neutrino Interactions with Kiloton-Scale Scintillation Detectors*; JINST, Volume 9 (2014); arXiv:1307.5813
 - [17] E. Oberla, J.-F. Genat, H. Grabas, H. Frisch, K. Nishimura, and G. Varner;
A 15 GSa/s, 1.5 GHz Bandwidth Waveform Digitizing ASIC;
Nucl. Instr. Meth. A735, 21 Jan., 2014, 452;
 - [18] E. Oberla and H.J. Frisch; *Charged particle tracking in a water Cherenkov optical time-projection chamber*; Nucl. Instr. Meth. Phys. Res. A814, 19 (April 2016); ISSN 0168-9002; arXiv:1510.00947
 - [19] P. Moskal, T. Bednarski, et al.; *TOF-PET Detector Concept Based on Organic Scintillators*; Nuclear Med Rev 2012; 15, suppl. C: C81-C84
 - [20] J.F. Shida, E. Spieglan, B.W. Adams, E. Angelico, K. Domurat-Sousa, A. Elagin, H. J. Frisch, P. La Rivière, A. H. Squires;
Ionization-activated Multi-State Low-Z Detector Media
arXiv e-Print: 2108.01715 (Aug 3, 2021); Nucl. Inst. and Meth. A; Volume 1017, 21 November 2021, 165801; <https://doi.org/10.1016/j.nima.2021.165801>
This contains an extensive bibliography, which is consequently not included here.

- [21] H. J. Frisch, E. J. Oberla, H.-J. Kim, M. Yeh; *Positron-Emission Tomography Detector Systems Based On Low-Density Liquid Scintillators And Precise Time-Resolving Photodetectors*// U.S. Patent 10,132,94, Filed April 8, 2016; Issued Nov. 20, 2018
- [22] M. Schever; *Status of the Jiangmen Underground Neutrino Observatory*; Ukrainian Journal of Physics, 64(7), 635; <https://doi.org/10.15407/ujpe64.7.635>
- [23] M.J. Berger, et al.; Photon Cross Sections Database; cross section data for Carbon, NIST Standard Reference Database 8; National Institute of Standards and Technology, Gaithersburg, Md, NBSIR 87-3597 (2010); <https://dx.doi.org/10.18434/T48G6X>. Also see reference [40], Fig. 33.15.
- [24] D. A. Glaser, *Some Effects of Ionizing Radiation on the Formation of Bubbles in Liquids*; Phys. Rev. 87 (4): 665 (1952)
- [25] B. Faddegon, J. Ramos-Mendez, J. Schuemann, J. Shin, J. Perl, H. Paganetti *The TOPAS tool for particle simulation, a Monte Carlo simulation tool for physics, biology and clinical research* European Journal of Medical Physics; Volume 72, P114-121, April (2020); DOI:<https://doi.org/10.1016/j.ejmp.2020.03.019>
- [26] E. Oberla, *Charged Particle Tracking in a Water Cherenkov Optical Time Projection Chamber*, Ph.D Dissertation, University of Chicago, Aug. 2015
- [27] H. J. Frisch; *Drifting Photons on Optical Paths, Mirrors, Sub-mm Resolution in Four Dimensions, and Transverse/Longitudinal Phase Space: Exploiting Psec Time Resolution*. Proceedings of the 5th International Conference on Micro-Pattern Gas Detectors (MPGD2017); 22-26 May, 2017, Philadelphia, USA; Proceedings in Science, 2018
- [28] Harvard is proud: He kept his pants on.
- [29] Segars WP, Sturgeon G, Mendonca S, Grimes J, Tsui BM. 4D XCAT phantom for multimodality imaging research. Med Phys. 2010 Sep;37(9):4902-15. doi: 10.1118/1.3480985. PMID: 20964209; PMCID: PMC2941518.
- [30] ICRP, 2002. Basic Anatomical and Physiological Data for Use in Radiological Protection Reference Values. ICRP Publication 89. Ann. ICRP 32 (3-4).
- [31] ICRP, 2009. Adult Reference Computational Phantoms. ICRP Publication 110. Ann. ICRP 39 (2).
- [32] ICRP, 2020. Adult mesh-type reference computational phantoms. ICRP Publication 145. Ann. ICRP 49(3).
- [33] Photon, Electron, Proton and Neutron Interaction Data for Body Tissues, ICRU Report 46. International Commission on Radiation Units and Measurements, Bethesda, 1992.
- [34] Hamamatsu Corporation Technical note MPPC modules, March 2021; See [Hamamatsu_mppc_modules_kacc9019e.pdf](#)
- [35] RISC

- [36] Minot M. J., et. al. *Large area picosecond photodetector (LAPPDTM) offers fast timing for nuclear physics and medical imaging*, Submitted for publication in "Il Nuovo Cimento" January 9, 2020
- [37] Christian Buck, private communication
- [38] M. Schever; *Status of the Jiangmen Underground Neutrino Observatory*; Ukrainian Journal of Physics, 64(7), 635; <https://doi.org/10.15407/ujpe64.7.635>
- [39] Christian Buck and Minfang Yeh. Metal-loaded organic scintillators for neutrino physics; Journal of Physics G: Nuclear and Particle Physics, 43(9):093001, 2016.
- [40] See D. Groom and S. Klein, LBNL Particle Data Group; <https://pdg.lbl.gov/2019/reviews/rpp2018-rev-passage-particles-matter.pdf>
- [41] D. Amidei et al.; *A Two-level Fastbus-Based Trigger System for CDF*; Nucl. Instr. and Meth. A269, 51 (1988)
- [42] E Angelico, A Elagin, HJ Frisch, M Wetstein;
Measuring the Neutrino Event Time in Liquid Argon by a Post-Reconstruction One-parameter Fit
Whitepaper submitted to Snowmass2021, <https://snowmass21.org/submissions/nf>
arXiv preprint 2004.00580 1 April, 2020
- [43] E. Spieglan; *Using Switchable Fluorescent Molecules to Image Tracks and Measure Energy in Large Liquid Double Beta Decay Detectors*; CPAD 2019; <https://agenda.hep.wisc.edu/event/1391/timetable/#20191209.detailed>
- [44] See the bibliography of Ref. [20].
- [45] M. Kono, H. Yamashita, K. Kubota, T. Kano, and A. Mimori
FDG PET Imaging in Pneumocytis Pneumonia
Clinical Nuclear Medicine 40, 8 Aug. 2015